A new on-line method for lithium plating detection in Lithium-ion batteries

Upender Rao Koleti [1]*, Truong Quang Dinh[1], James Marco[1]

[1] *WMG, The University of Warwick, Coventry CV4 7AL, United Kingdom*

Abstract

The desire to move towards the rapid charging of lithium-ion batteries has motivated many researchers to understand the underpinning degradation mechanisms as a precursor for the design of novel models and control algorithms to help mitigate their occurrence. It is widely reported that lithium plating is a significant ageing mechanism that occurs when charging the battery at low temperatures, high C-rates and high state of charge (SOC). There are multiple efforts embracing the measurement of different parameters during charging, such as battery voltage and current, that may collectively provide critical information useful for the detection of lithium plating. Much of this research is focussed on the post-processing of such data after completion of charge to infer the onset of lithium plating. This study aims to extend recent work, by proposing a new method of lithium plating detection, based on an estimation of cell impedance. This approach is able to operate in real-time during charging and therefore transferable to the battery management system (BMS). Experimental results highlight that the proposed method is highly sensitive and capable of effectively detecting the onset of lithium plating in real-time, underpinning the design of future optimal charging strategies to minimise lithium plating.

Keywords: Lithium Plating; Fast Charging; Lithium-Ion; Battery Impedance, Battery Management System

Terms and Abbreviations

BMS	Battery Management System
CC	Constant Current
CCCV	Constant Current Constant Voltage
CTL	Charge Transfer Limitations
CV	Constant Voltage
DV	Differential Voltage
EIS	Electrochemical Impedance Spectroscopy
EV	Electric Vehicle
ZTR	Impedance at the transition frequency f_{tr}
ZTR	Resistive part of the ZTR
ICP-OES	Inductively Coupled Plasma Optical Emission Spectrometry
NE	Negative Electrode
NEP	Negative Electrode Potential
NMC	Nickel Manganese Cobalt Oxide
NMR	Nuclear Magnetic Resonance
NCA	Lithium Nickel Cobalt Aluminium Oxide
OCV	Open Circuit Voltage
PE	Positive Electrode
SDL	Solid Diffusion limitations
SEI	Solid Electrolyte Interphase

* Upender Rao Koleti. Tel.:+44-7471114926; *E-mail address*: u.koleti@warwick.ac.uk.

SOC	State of Charge
VRP	Voltage Relaxation Profiles

Symbols

f_{tr}	Transition frequency (Hz)
f_{max}	Frequency at which reactance attains maximum level in the mid-frequency region (Hz)
I_c	Critical cut-off current of the CV phase (A)
I_{ch}	Charge current (A)
I_{in}	Intercalating current (A)
I_{li}	Lithium plating current (A)
Li_{NES}	Lithiation level of the negative electrode at its surface
Li_{PES}	Lithiation level of the positive electrode at its surface
Q_{nom}	Battery *capacity* (Ah)
τ	Time constant (s)
$V_{NE,S}$	Potential of the negative electrode at its surface (V)
$V_{PE,S}$	Potential of the positive electrode at its surface (V)
Z_{Ω}	Impedance of the current collectors (Ω)
Z_{CTL}	Impedance of the charge transfer limitations (Ω)
Z_{EI}	Impedance of the electrolyte (Ω)
Z_{SDL}	Impedance of the Solid diffusion limitations (Ω)
Z_{SEI}	Impedance of the solid electrolyte interphase (Ω)

1 Introduction

A number of studies advocate the use of lithium-ion (Li-ion) batteries, as an energy storage solution, due to their low weight, high energy density and long service life [1, 2]. Within Li-ion batteries, there are many variants that employ different types of negative electrode (NE) materials such as graphite [3, 4] and lithium titanium oxide (LTO) [5, 6]. Among them, graphite-based Li-ion batteries are less expensive and offer high energy densities [7]. Although Lithium-ion batteries with graphite have been widely used in portable electronic devices, such as mobile phones and laptops, challenges are still remained and need to be addressed in order to meet the stringent requirements of the automotive industry and to facilitate their introduction within future electric vehicles (EVs) [8, 9]. One such requirement is the need to charge the EVs battery system at relatively high current rates under a diverse range of ambient temperatures [10].

It is widely reported that charging at high C-rates or at low ambient temperatures accelerates degradation when the Li-ion battery comprises of a graphite-based NE [3, 4]. The limiting factor is reported to be the deposition of metallic lithium on the NE surface that occurs when the NE potential (NEP) reduces below the lithium reference potential because of the reduced kinetics (such as a reduced intercalation and increased interfacial potential drops [4, 11]). Lithium plating decreases the amount of cyclable lithium between the electrodes that manifests itself as a reduction in capacity at a cell level. In addition, deposited lithium metal may grow through the separator, in the form of dendrites, which can result in an internal short circuit causing thermal runaway. This represents a significant safety concern for many end-users [12]. To ensure the safe and durable use of lithium-ion batteries, optimisation of the charging protocols is therefore required for the effective control of lithium plating when charging the battery at low temperatures or high C-rates.

To avoid or reduce the amount lithium plating, it is essential to detect its onset during a charging event. Estimation of its occurrence is typically underpinned by electrochemical models where the NEP is expressed by a set of partial differential equations (PDEs) based on the electrochemical and physical properties of the battery components such as the electrodes and electrolyte [13, 14]. To reduce the complexity of these models for real-time use, reduced-order models are suggested in the literature to quantify the NEP to predict the onset of lithium plating [13]. However, material properties and thus the magnitude of the potential drop at the NE will undergo changes as the cell ages, due to a number of degradation mechanisms such as: electrolyte decomposition, solid electrolyte interface (SEI) layer growth, loss of active material and porosity changes due to SEI growth and previously deposited lithium metal layers [15, 16]. In addition, the non-homogeneities in the cell construction or packaging variations of the cell within the complete battery pack (such as varying compression levels in the cell) can lead to localized plating [17, 18]. These effects further compound the significant research challenge of

extending these models to consider the different degradation modes and to accurately employ them to represent the battery in a form that is computational efficient for inclusion within the battery management system (BMS) [16, 19].

There are multiple ex-situ techniques reported in the literature for lithium plating detection, such as nuclear magnetic resonance (NMR) and inductively coupled plasma optical emission spectroscopy (ICPOES) [1, 20]. However, these methods are not suitable for real-time charging control because of the difficulty in quantifying lithium plating "cycle by cycle" and the ultimate need for cell disassembly as part of the assessment process. Further, these methods detect the irreversible part of lithium plating and do not support the identification of the cell voltage or state of charge (SOC) level at which lithium plating commences during a charging event.

Table 1: Summary of li-ion plating detection strategies within context of possible BMS deployment

Category	Methodology	Primary advantages and disadvantages to real-time BMS deployment
Ex-situ	NMR and ICPOES [1, 20]	Cell disassembly limit their use for real-time implementation
In-situ	Tomography [21]	Neutron diffraction analysis is not suitable for real-time use
	Differential curves [16, 22] Voltage relaxation profiles [23]	Application of these methods need specific operating conditions CV cut-off current and temperature influence the detection sensitivity Cannot detect the onset of plating within a charging event

A number of in-situ lithium plating detection methods including tomography [21], Differential voltage (DV) curves [16, 22] or Voltage Relaxation Profile (VRP) methods [21, 24] can be found from the literature. Among them, the tomography approach that employs neutron diffractions to track changes in the lithiation level cannot be used for designing BMS because of the significant instrumentation it requires that would be prohibitive for many applications [21, 25]. The DV and VRP approaches offer the advantage that they only employ the on-board measurable parameters (e.g. voltage and current) to infer the onset of lithium plating. However, the constant discharge current needed for the DV curve method and a considerable relaxation period (in excess of 1 hour) needed for the VRP method after a charging event limit their use in real-time applications. Additionally, these in-situ methods that detect reversible part of lithium plating are sensitive to the cut-off current of the constant voltage (CV) charge period [22, 26]. Lithium stripping or intercalation of the reversible part of lithium plating can begin in the CV phase of the charging period itself. Subsequently, terminating the charge at a current level (referred to as the critical cut-off current, I_c within [26]) where lithium stripping begins would allow the total amount of reversible lithium plating available for detection [22, 23]. Nevertheless, identifying I_c at different temperatures, charge C-rates and ageing levels

needs a careful and sensitive analysis as described in [23] and may be difficult to implement within practical control system applications. Hence, it is argued that none of the existing methods found in the literature could detect the onset of lithium plating while the battery is undergoing a charge-event and is real-time implementable. In summary, the different in-situ and ex-situ detection methods of lithium plating, reported in the literature are summarised in Table 1 within context of possible BMS deployment.

The challenge of determining the onset of lithium plating during charge remains prominent for many battery applications. The objective of this research is to develop and validate an in-situ method for detecting the onset of lithium plating in a commercial cell during charge using standard battery health monitoring signals (e.g. voltage and current) which is also implementable for real-time use. The research hypothesis is to detect lithium plating by tracking battery impedance during a charge event. Concentration gradients in the electrodes and electrolytes, SEI layer, Ohmic resistance of the current collectors and charge transfer limitations (CTL) at the electrode interface collectively contribute to the value of battery impedance. It is assumed that a new process introduced by lithium plating in the form of lithium metal depositions at the NE will modify the battery impedance profile. It is therefore believed that lithium plating shall be identifiable by tracking the impedance profile during charge.

During experimentation, cell impedance is monitored during a charge event at different temperatures and C-rates by introducing a disturbance to the charge current and measuring the resulting voltage change. A distinct impedance profile is observed under the influence of lithium plating which is subsequently confirmed through the application of the VRP method. In contrast to existing lithium plating detection methods that detect either the reversible or irreversible part in post-charge conditions, the proposed method identifies the onset of lithium plating actually during charging in a non-destructive manner. It is argued that the proposed method will be useful to derive the charging strategies online since the value of charging current can be modified once the onset of plating is detected to mitigate its growth.

The remainder of this paper is structured as follows. The theoretical background for the consideration of impedance for plating detection is detailed in Section 2. Section 3 discusses the experimental framework and methodology. Section 4 presents the experimental results to highlight the potential of the proposed method. Overall conclusions of this study and outlines for future work are provided in the final section.

2 Methodology

This section presents the theoretical background of the proposed impedance-based lithium plating detection method. First, multiple processes internal to the battery that underpin the measure of impedance to the charge flow are discussed along with the use of electrochemical impedance spectroscopy (EIS) techniques for their quantification. Second, the potential influence of lithium plating on the impedance of

a subset of processes are discussed. Next, a method to detect this change to the impedance profile in order to identify lithium plating is presented.

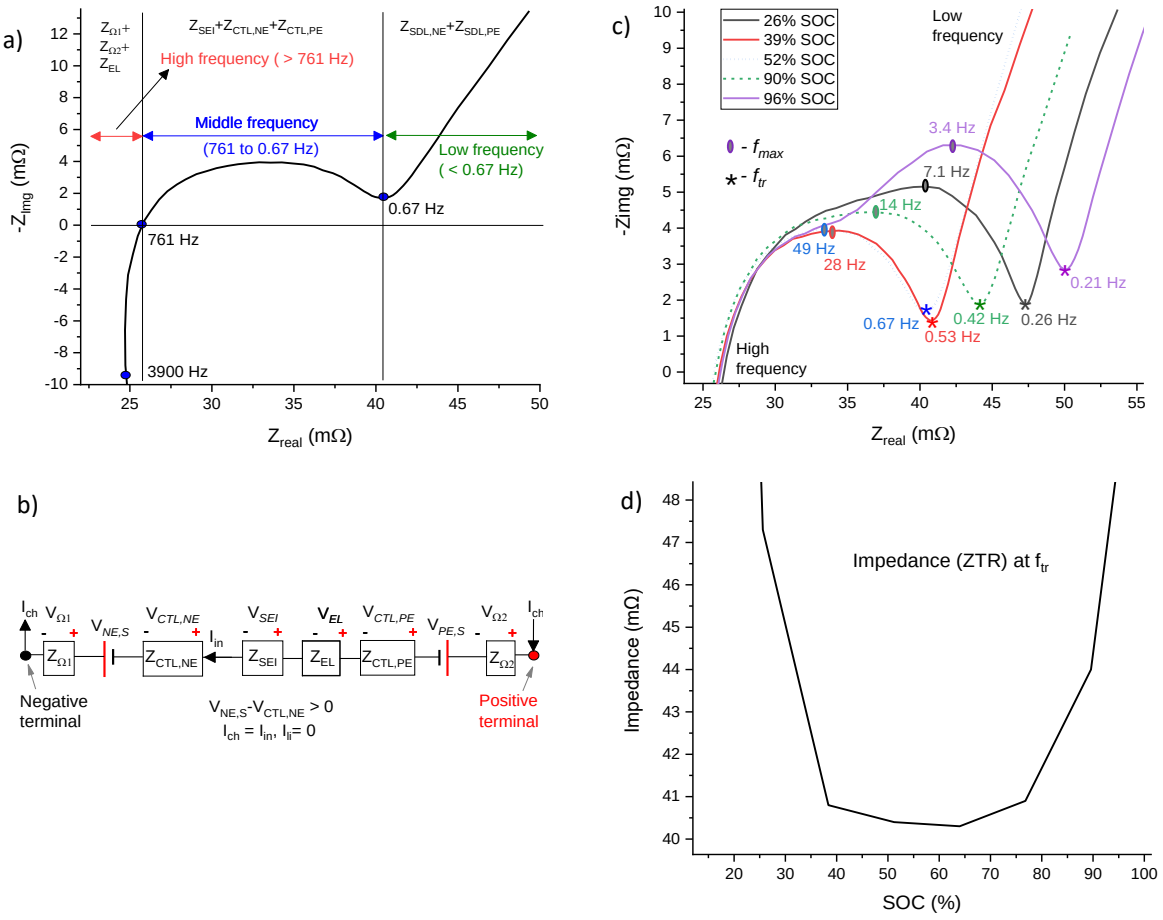

Figure 1: Battery impedance: a) EIS plot at 50% SOC, b) Equivalent electrical circuit diagram representation of the battery impedance, c) EIS plots at different SOC levels and d) impedance and resistance at the transition frequency f_{tr}

2.1 Battery impedance

Lithium exchange between the electrodes in a lithium-ion battery comprises of a series of multiple processes including lithium-ion diffusion in the electrolyte, migration through the SEI layer, charge transfer through the electrode/electrolyte interface, solid-state diffusion in the bulk of active material and electron transfer external to the battery via the current collectors [27, 28]. During charge/discharge events, these processes introduce impedance to the charge flow and cause a voltage drop between the two electrodes. As discussed within [28], these processes can be individually identified by using EIS since each of them has a different time constant or frequency range of excitation.

Commercially available 18650-type lithium-ion cells with a rated capacity of 3.1Ah are used in this study. The NE material of the cell is graphite and the positive electrode (PE) material is $LiNiCoAlO_2$, commercially known as NCA. Figure 1a shows the EIS plot of a new cell of the selected cell type at 50% SOC after it has been allowed to equilibrate for 4 hours at room temperature (25 °C). A number of publications such as [27, 29] describe in detail how to interpret the EIS plot and so this information will not be repeated here.

However, for completeness, a brief summary is provided below. As discussed within [28], the high-frequency region (≥761 Hz) is caused by the ionic conduction through the electrolyte and electronic conduction through the current collectors whose impedances are represented by Z_{EL} and Z_{Ω} respectively. The mid-frequency region (between 761 and 0.67 Hz) represents the charge transfer limitations (CTL) at the electrode-electrolyte interfaces and the ion migration through the SEI layer whose impedances are represented by Z_{CTL} and Z_{SEI} respectively. The low-frequency part (<0.67 Hz), usually characterised by a 45° slope, is introduced by the solid diffusion limitations (SDL) in the electrodes. Figure 1b shows the equivalent circuit of a lithium-ion battery by this network of impedance values. In the figure, the impedance due to SDL (referred as $Z_{SDL,NE}$ or $Z_{SDL,PE}$) at each electrode is hidden under the electrode surface potential represented by $V_{NE,S}$ or $V_{PE,S}$ that is different from open-circuit voltage (OCV) due to the potential drop introduced by the SDL.

Figure 1c shows the EIS plots of the same cell at different SOC levels. As it can be observed and as reported within [28], impedance in the mid-frequency range varies with SOC. Since Z_{CTL} and Z_{SEI} contribute to this range and since no significant change in the SEI layer thickness is expected in a single charge/discharge cycle [30, 31], the mid-frequency impedance variations can be attributed largely to the Z_{CTL}. The electrochemical models that describes the CTL through the Butler-Volmer equation [32, 33] also support this rationale. According to their presented analysis, Z_{CTL} at an electrode varies according the electrode surface lithiation level. At low (near to 0 %) and high lithiation levels (near to 100 %), Z_{CTL} is high and reduces as the lithiation level moves towards 50%. Therefore, the impedance changes in the mid-frequency region comes mainly from the Z_{CTL} and tracking the battery impedance should indicate the way Z_{CTL} is changing while the battery is being charged or discharged. The influence of lithium plating on the Z_{CTL} and detection of onset of lithium plating with the help of Z_{CTL} are detailed in section 2.2.

The impedance measured at the transition frequency (referred as f_{tr} which is marked with "*" in Figure 1c) at which impedance changes to 45° slope allows quantifying the total impedance from both the high and the mid-frequency regions. Since the impedance from the high-frequency region is nearly constant (as seen from Figure 1c), tracking the impedance at the f_{tr} (referred as ZTR) allows tracking the mid-frequency impedance changes and thus Z_{CTL}. ZTR measured at the f_{tr} can be estimated as:

$$ZTR = Z_{\Omega} + Z_{CTL} + Z_{SEI} + Z_{El} \qquad (1)$$

$$\textit{where} \quad Z_{\Omega} = Z_{\Omega 1} + Z_{\Omega 2} \; and \; Z_{CTL} = Z_{CTL,NE} + Z_{CTL,PE}$$

Here, $Z_{\Omega 1}$ and $Z_{\Omega 2}$ are Ohmic resistances at the NE and PE respectively; $Z_{CTL,NE}$ and $Z_{CTL,PE}$ are impedance due to CTL at the electrodes NE and PE respectively. Figure 1d presents the ZTR profile against the battery

SOC where ZTR drops initially as battery SOC raises from 0% and reaches a near flat level in the mid-SOC range before rising again as SOC goes further towards 100%.

2.2 Impedance tracking with EIS

The approach taken to track the ZTR and thus Z_{CTL} while charging/discharging without the use of laboratory equipment requires interrupting the current or creating a step change to the current similar to the hybrid pulse power characterization (HPPC) test often used in developing equivalent circuit models [34, 35]. In this work, charge current is interrupted every 1% SOC increase for a predefined time period. The step-change in the current and the associated voltage change during the interruption is used to calculate the real part of ZTR (referred as RTR) based on Ohms law. To understand how RTR enables the ZTR tracking, the following discussion is provided.

As seen from Figure 1c, the imaginary part of the impedance or reactance at f_{tr} is significantly lower than the resistive part (RTR) irrespective of the SOC level. Table 2 shows the ZTR (or impedance at f_{tr}) and its real part along with the reactance at different SOC levels. Here, RTR is found to be within 1% of the total value of ZTR irrespective of the SOC level. Therefore, variations in the mid-frequency impedance or the ZTR can be tracked using the calculated RTR value.

Table 2: Impedance and its reactive and resistive parts at f_{tr}

SOC (%)	f_{tr} (Hz)	RTR (mΩ)	Img (ZTR) (mΩ)	ZTR (mΩ)	RTR/ZTR*100
26	0.21	47.3	1.89	47.33	99.94
39	0.54	40.8	1.43	40.82	99.95
52	0.67	40.5	1.69	40.53	99.93
78	0.67	40.9	1.61	40.93	99.93
96	0.16	50.2	2.86	50.28	99.84

To identify the charge interruption time period, as discussed within [28], the time constant (τ) of an equivalent RC network that produces the semi-circle in the mid-frequency region can be used. The value of τ is calculated with the frequency (referred as f_{max} which is marked with circles in Figure 1c) at which the imaginary part of the impedance attains a maximum level in the mid-frequency region using $\tau = (2\pi f_{max})^{-1}$. An interruption time of 2τ s shall recover the voltage drop due to the RC network by 87% of the maximum value [28].

2.3 Impedance under lithium plating

While charging at low C-rates or during high ambient temperatures, due to the improved diffusion in the electrodes, differences between the lithiation levels of the electrode surface (referred as Li_{NES} and Li_{PES} for the NE and PE respectively) and the bulk are known to reduce [32, 33]. Therefore, charging conditions that

allow Li_{NES} and Li_{PES} closer to their average electrode lithiation levels can produce a ZTR profile similar to the ZTR profile obtained from the EIS measurements taken at different SOC levels (as seen from Figure 1d) where the lithiation differences in the electrode particles are deemed to be negligible. Conversely, at high C-rates of charging or at low temperatures, the rate of Li_{NES} rise in line with SOC increases because of increased SDL or reduced diffusion in the electrodes. Therefore, the Z_{CTL} that depends on the Li_{NES} can reach the lower levels at a lower SOC level compared to charging at low C-rates or high temperatures. With further charging, Li_{NES} tends to raise towards a full lithiation level as $V_{NE,S}$ comes closer to Li reference potential much before the battery reaches 100% SOC. Besides, the potential drop due to CTL (referred as V_{CTL}) that increase with increasing C-rate or decreasing temperature when combined with the lower potential of $V_{NE,S}$ can push the NE potential below the Li reference where lithium plating commences. Once lithium plating begins, the rate of electrode lithiation rise is reduced and accordingly the Z_{CTL} rise is reduced since the charging current (referred as I_{ch}) is now divided into intercalating current (referred as I_{in}) and lithium plating current (referred as I_{li}). Additionally, as discussed within [13, 20], the lithium plating reaction at the NE also follows the Butler-Volmer equation that introduces a new branch of impedance in parallel to the existing $Z_{CTL,NE}$ as shown in Figure 2. Similar to intercalating current that faces $Z_{CTL,NE}$, lithium plating current faces an impedance referred here as $Z_{CTL,Li}$. As a result, the overall impedance at the NE drops compared to $Z_{CTL,NE}$ after the onset of lithium plating. On this basis, it is hypothesised that tracking the ZTR will allow detecting the onset of lithium plating during the charge event.

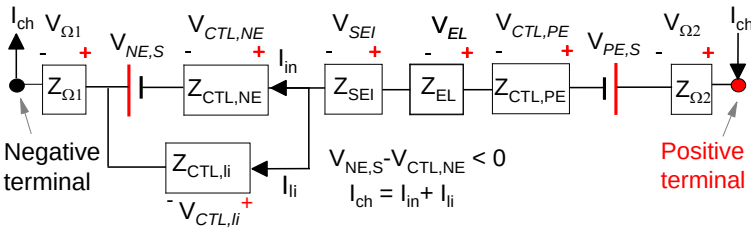

Figure 2: Equivalent circuit representation of a battery impedance after the onset of lithium plating

The hypothesis to detect lithium plating can be further explained as follows. In the case of a charging event without lithium plating, ZTR or Z_{CTL} follows the curve from Figure 1d where ZTR faces continuously decreasing reduction at lower SOC levels to reach a near flat level in the mid-SOC range and then accelerate as SOC rises towards 100%. In the case of a charging event with lithium plating, ZTR faces a second downtrend after the onset of lithium plating because of the introduction of parallel impedance ($Z_{CTL,li}$) across the existing $Z_{CTL,NE}$. Detecting this second downward trend by tracking the ZTR shall, therefore, indicate the onset of lithium plating.

2.4 Impedance tracking in real-time

To track ZTR using a charge interruption technique while the battery is undergoing a charge event, f_{max} that varies with SOC, temperature and ageing must be known priori. As seen from Figure 1c, f_{max} and f_{tr} levels vary from circa 3.4 to 49 Hz and 0.21 to 0.67 Hz respectively with SOC for the new cell selected while testing at 25°C. As per [28], the values of f_{max} and f_{tr} can reduce as low as in turn to 100 mHz and 10 mHz for a comparative aged cell while testing at 0 °C temperature although these numbers vary between cell type according to the cell format and chemistry [36]. Since it is difficult to identify f_{max} or f_{tr} in real-time applications to track impedance of the mid-frequency region, a fixed frequency approach is adopted in this work. Implications of using a fixed frequency against the variable f_{tr} on ZTR tracking is analysed using the EIS data.

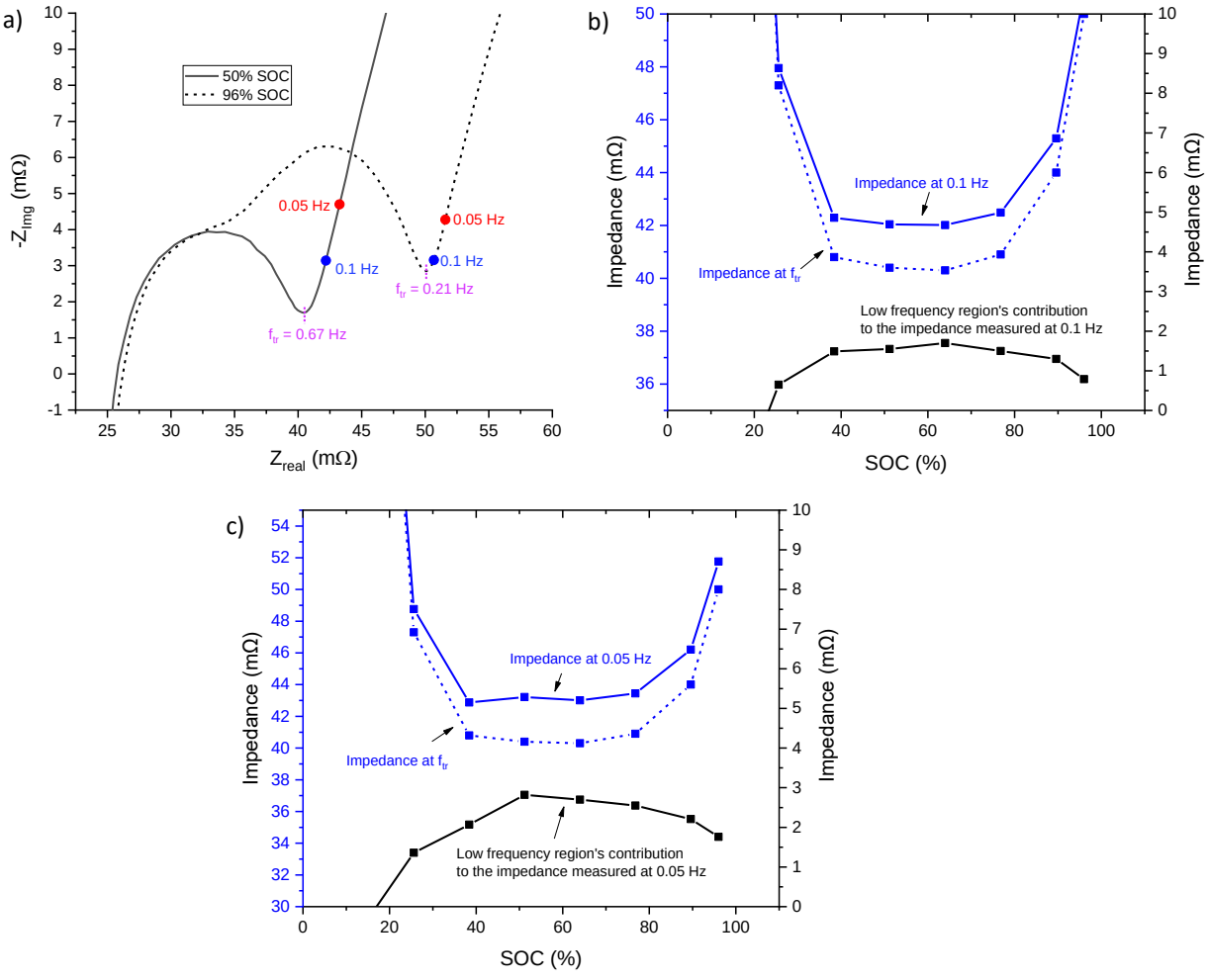

Figure 3: Battery impedance: a) EIS plots marked frequencies f_{tr}, 0.1 and 0.05 Hz; b) impedance profile at 0.1 Hz in comparison with that of f_{tr} along with the impedance from the low-frequency region at 0.1 Hz and c) impedance profile at 0.05 Hz in comparison with that of f_{tr} along with the impedance from the low-frequency region at 0.05 Hz

Selecting a frequency level that falls in the low-frequency region and that is below the f_{tr} range shall not only facilitate tracking of the impedance from the mid-frequency region but also some portion of low-frequency region as well. For the observed f_{tr} range of 0.67 and 0.21 Hz, the impact of fixing the frequency

of AC excitation at 0.1 Hz and 0.05 Hz is analysed to better understand whether the Z_{CTL} can be adequately quantified while employing this assumption. Figure 3a shows EIS plots marked with f_{tr}, 0.1 Hz and 0.05 Hz at 50 and 96% SOC levels. The impedance at 0.1 Hz and 0.05 Hz from the EIS measurements are plotted against the SOC as shown in Figure 3b and Figure 3c respectively along with that value of the f_{tr}. The impedance profile at 0.1 Hz is found with some offset compared to the ZTR profile obtained at f_{tr}. Impedance from the low-frequency region (termed Z_{low}) at 0.1 Hz is combined with that of ZTR to produce an offset as seen from Figure 3b. The impedance at 0.1 Hz is able to produce a profile similar to that of the ZTR for two reasons.

- First, the contribution of the low-frequency region to the overall impedance value at 0.1 Hz is less than 5% of the overall ZTR value. As seen from Figure 3b, the minimum level of ZTR (or impedance at f_{tr}) and maximum level of the Z_{low} are circa 40 and 1.8 mΩ respectively.
- Second, the rate of impedance change experienced by the ZTR is much higher than that of the Z_{low}. For example, an increment in the value of ZTR and decrement in the value of Z_{low} are in turn 9.1 and 0.8 mΩ while the SOC is rising from 78 to 96%. As a result, the impedance at 0.1 Hz is still able to maintain the initial drop and final rise and able to produce a profile similar to that of ZTR. Similar results are observed for the impedance profile at 0.05 Hz (Figure 3c). To summarise, the ZTR profile can be tracked with a chosen frequency that is below the f_{tr} range.

Similarly, the value of charge interruption time derived from a frequency that is below the f_{max} range can ensure tracking of the impedance from the mid-frequency region in all operating conditions. Since the minimum level of f_{max} for the new cell is observed at 3.4 Hz and it can decrease further with reducing temperatures and increasing ageing levels [28], a minimum f_{max} level of 100 mHz is considered to derive the rest period. At the identified reference frequency (f_{max}), τ is 1.59 s ($\tau = (2\pi f_{max})^{-1}$) and measuring the voltage response in 3 s allows us to measure 85% of the total change expected. As a result, to study lithium plating by tracking the impedance, charge currents are interrupted for 3 s for every 1% SOC increase. The experimental procedures to track ZTR using the intermittent charge interruption are detailed in section 3.

3 Experimental

To track the value of ZTR during different charging events that include potentially non-plating and plating conditions, experiments at different ambient temperatures (10, 20 and 30 ^{o}C) and C-rates (0.2, 0.5, 0.75, 1 and 1.25C) are performed. For the selected cell type, the recommended maximum charge C-rate is 0.42 C (or 1.25 A) and a charge temperature range defined as 10 to 45 ^{o}C. Therefore, charge C-rates higher than 0.42C may be deemed “abusive” and could potentially cause lithium plating even within the recommended temperature range [1, 16]. A detailed description of the experimental setup and test procedure are presented in the following sections.

Table 3: Cell level test cases

Test case	Temperature	charge C-rates
Set A: 3 cells	10^{o}C with active cooling	0.2C, 0.5C, 0.75C, 1C, 1.25C
Set B: 3 cells	20^{o}C with active cooling	0.2C, 0.5C, 0.75C, 1C, 1.25C
Set C: 3 cells	30^{o}C with active cooling	0.2C, 0.5C, 0.75C, 1C, 1.25C
Set D: 3 cells	20^{o}C without active cooling	0.2C, 0.5C, 0.75C, 1C, 1.25C

3.1 Test case definition

Four test cases employing four sets of cells are employed for experimentation. For each test case, as shown in Table 3, three cells are selected for reproducibility and to minimize the influence of cell-to-cell variations on the experimental results. Among them, test cases A, B and C are performed at 10, 20 and 30^{o}C respectively to study the ZTR profile at different C-rates at each temperature with active cell surface cooling. In addition, test case D is included in the experimental programme to analyse the impact of temperature rise during charge on the ZTR profile where the cells are operated without active cell surface cooling.

Table 4: Measurement parameters and their range and accuracies

Measuring parameter	Operating range	Measurement accuracy	Resolution	Sampling time
Cell voltage	2.7 to 4.2 V	± 1 mV	0.1 mV	20 ms
Cell current	+4.8 to -1 A	± 1 mA%	0.030 mA	20 ms
Cell temperature	0 to 30 ^{o}C	± 1 ^{o}C	0.01 ^{o}C	1 s

3.2 Experimental setup

In this work, the selected cells are placed on a Perspex plate fixture through which the cells are connected to a Maccor cell cycler (Model: Series 4200). To keep the cell temperature as close as possible to the desired temperature (except for case D), liquid (Kryo 51 silicon oil) cooling over the cell surface is used with the support of a LAUDA (Model: Proline RP 845 C) temperature Controller. In the case of test case D, cells are evaluated in an environment maintained at 20^{o}C without any active cooling to allow the usual rise of temperature during charge. For the analysis, the Maccor unit enables data recording of the cell voltage and current with ±0.1 mV and ± 0.03 mA resolutions, respectively. Furthermore, a Maccor probe using T-type thermocouples with an accuracy of ±1 °C is placed at the centre of the cell in the axial direction to measure temperatures on the cell surfaces. The test parameters including the measurement accuracies and sample rates are summarised in Table 4.

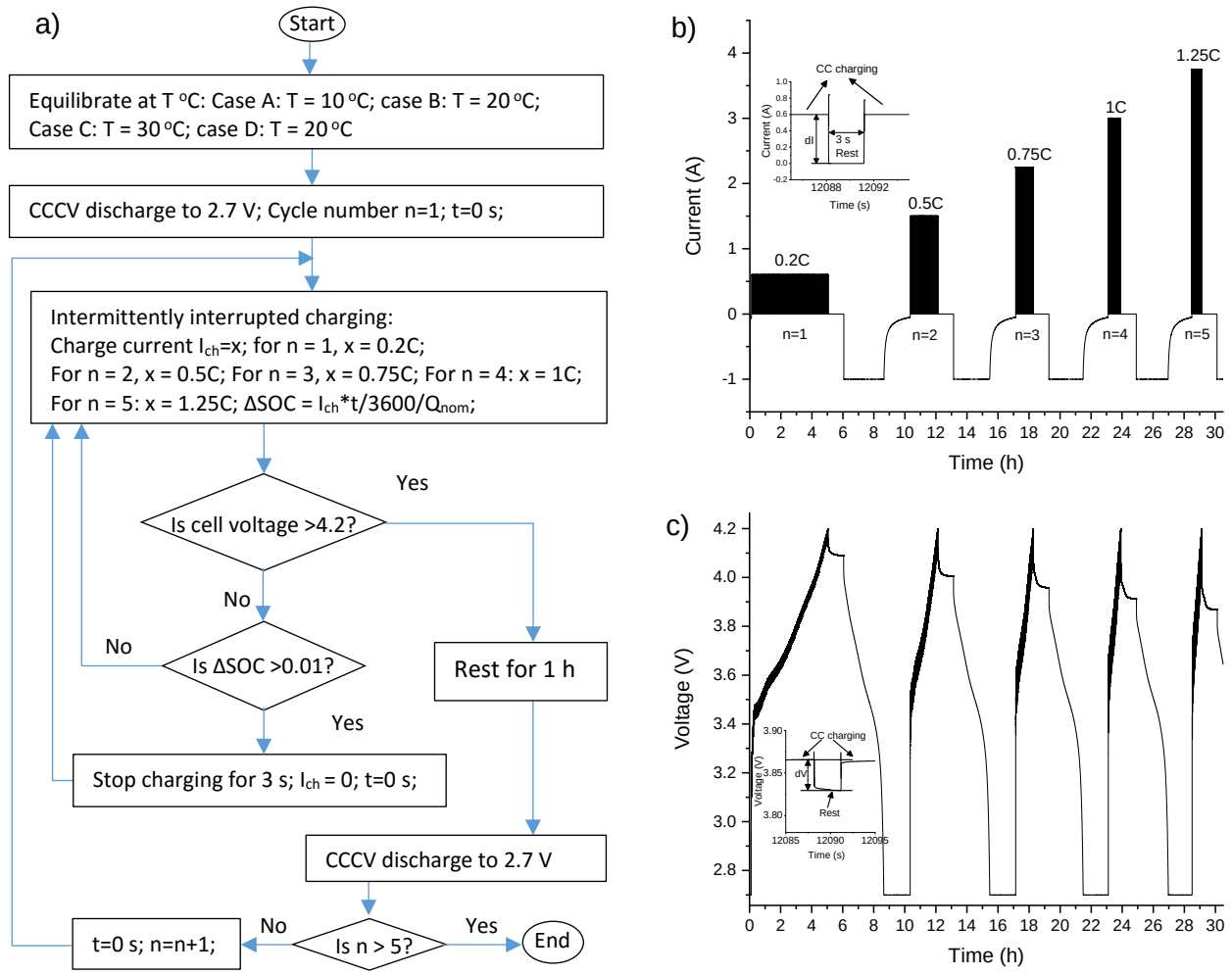

Figure 4: Experimental procedure: a) flow chart, b) current and c) voltage profiles in charge interruption tests

3.3 Experimental procedure

All the cells prior to the impedance tests are preconditioned for six cycles at 25°C temperature with C/3 constant current (CC) charge/discharge rates and C/40 constant voltage (CV) cut-off current between the voltage limits of 4.2 and 2.7 V. The SEI layer over the NE grows largely during the initial few cycles after which the rate of growth reduces as its layer thickness increases [37]. As a result, impedances due to the SEI layer attain stable levels after the preconditioning cycles as discussed further within [38]. The number of preconditioning cycles required to stabilize a cell may vary according to its chemistry and format. From our previous work [23], the selected cell type could reach stable capacity levels within the first 6 cycles of preconditioning. After the preconditioning stage, the impedance tests in each test case are performed at their selected temperature while charging. The test procedures are presented through a flow chart as shown in Figure 4a.

In each case, the cells are cycled five times with different charge rates in each cycle starting from 0.2C in the first cycle to 1.25C in the last cycle as shown in Figure 4a. Prior to each charge test, the cells are

discharged to 2.7 V with a CC-CV profile using a C-rate of C/3 in the CC phase and a CV cut-off current of C/40 in the CV phase. Then, the cells are charged with the modified CC charge (intermittent charge interruption) to estimate the values of ZTR in real-time. Since the focus of this work is to detect lithium plating that occurs during charge, application of the modified current profile is limited to charging events.

To track the profile of ZTR, the cells are charged incrementally, in steps of 1/100 of the nominal capacity ($Q = Q_{nom}/100$), by applying selected C-rate of charge and subsequently allowing the cell voltage to relax for three seconds *as discussed earlier*. Here Q_{nom} of the cell refers to the *discharge capacity* measured in the 6th cycle of preconditioning. Figure 4b and c show cell voltage and charge currents where positive and negative levels of cell current refer to charge and discharge respectively. The cell voltage recovery by the end of each rest period (referred as dV) and the current difference created (referred as dI) from the CC charge to the 3 s rest are recorded to calculate the resistance ZTR using Ohms law.

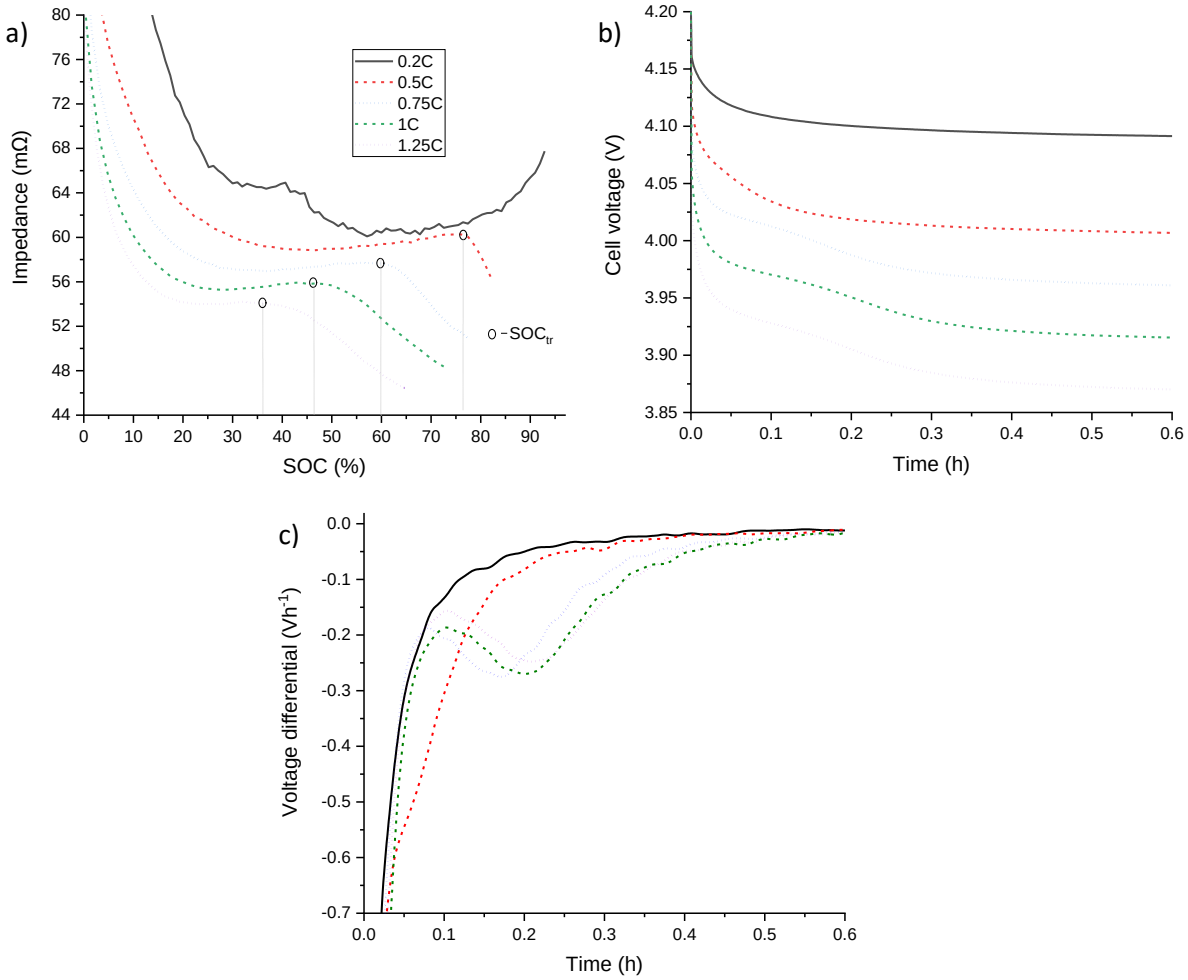

Figure 5: a) ZTR profiles of a cell in test case A (10 °C) at different C-rates (dotted vertical lines indicate the SOC level at which ZTR shows unusual trend. b) Post-charge voltage relaxation profiles and c) their differentials at different C-rates.

4 Results & Discussion

4.1 Charge at low C-rate

During charge, lithium is transferred from the PE to the NE. The lithiation level of the PE drops and that of NE rises as the charging event progresses. The ZTR that is influenced by the electrode lithiation levels is tracked as the charge progresses. For different current C-rates at 10 ^{o}C, Figure 5a shows the ZTR profiles plotted against the battery SOC. For the case of 0.2C charge rate, the ZTR reduced in the initial period of charging and then attained minimum levels in the mid-SOC band and then started to rise once again towards the end of charging. This profile is similar to the original ZTR profile (Figure 1d) obtained with the EIS data that is measured under non-plating conditions. Since the potential drops in the battery are expected to be significantly low while charging at a C-rate of 0.2C, the NEP could stay above the Li reference value for the entire charging period and thus, lithium plating is not expected in this low C-rate charging scenario. The absence of lithium plating is further confirmed with the VRP method that infers lithium plating using post-charge voltage relaxation profiles. A full description of the VRP method; its underpinning theory, derivation and application can be found from [21] and will therefore not be repeated here. Figure 5b and c show the voltage relaxation profiles and its differential respectively. As per the VRP method, the single-stage relaxation of the voltage or its differential without a valley and peak for the 0.2C charge indicates the absence of plating.

4.2 Charge at high C-rates

To observe the ZTR profiles at high charge C-rates and at a temperature of 10 ^{o}C where lithium plating could potentially occur, charge C-rates 0.5C, 0.75C, 1C and 1.25C are applied in sequence where the fully discharged battery is charged at the selected C-rate to 4.2V with the proposed charge interruption procedure. The ZTR profiles (as seen from Figure 5a) for charge rates ≥0.5C show an unusual trend compared to that of 0.2C or to the ZTR trend derived from the EIS data (Figure 1d). After reaching near flat levels in the middle of charging, the ZTR profile of 0.2C show a continuous rise until the end of CC charging. Conversely, the ZTR profiles for charges rates ≥0.5C have shown a negative trend until the end of CC charging period. The SOC level at which this trend begins (referred to as SOC_{tr} that is marked with vertical lines in Figure 5a) reduces with increasing C-rate which is in line with the general understanding, reported in the literature, that increasing C-rates reduce the SOC level at which lithium plating commences [10, 39]. As it can be seen from Figure 5a, SOC_{tr} is dropped from 79% at 0.5C charge rate to 35% at 1.25C charge rate.

As mentioned in section 2, the onset of lithium plating could affect the ZTR to produce such a negative trend. As discussed within [40] and described earlier, increasing charge C-rates raises the potential drops due to various internal mechanisms and lithium plating begins if the NEP drops below the Li reference level. The occurrence of lithium plating is confirmed with the VRP method. As shown in Figure 5c, the cell voltages

in the post-charge relaxation period exhibit a two-stage recovery and their differentials with peaks and valleys indicate the occurrence of lithium plating for the charge rates greater than 0.75C. In the case of 0.5C charge rate, the voltage differential (Figure 5c) shows a profile that neither indicates the absence (as in the case of 0.2C) or occurrence of plating (as in the case of 0.75C) potentially because of smaller levels of lithium plating that are not detectable using this method. Therefore, as validated by the VRP method and supported by the theory described in section 2, it is believed that the ZTR profiles can be used to detect the occurrence of lithium plating. Once lithium plating begins, the intercalating current drops that reduces the rate of Li_{NES} raise. Since ZTR or Z_{CTL} are strongly associated with the Li_{NES}, the Z_{CTL} raise is reduced. Further, with the introduction of a parallel reaction in the form of lithium plating at the NE surface, the Z_{CTL} comes in parallel with the plating induced impedance at the NE interface as described in section 2. As a result, the impedance at the NE surface drops compared to the Z_{CTL}. Therefore, the SOC_{tr} at which ZTR trend changes shall indicate the onset of plating.

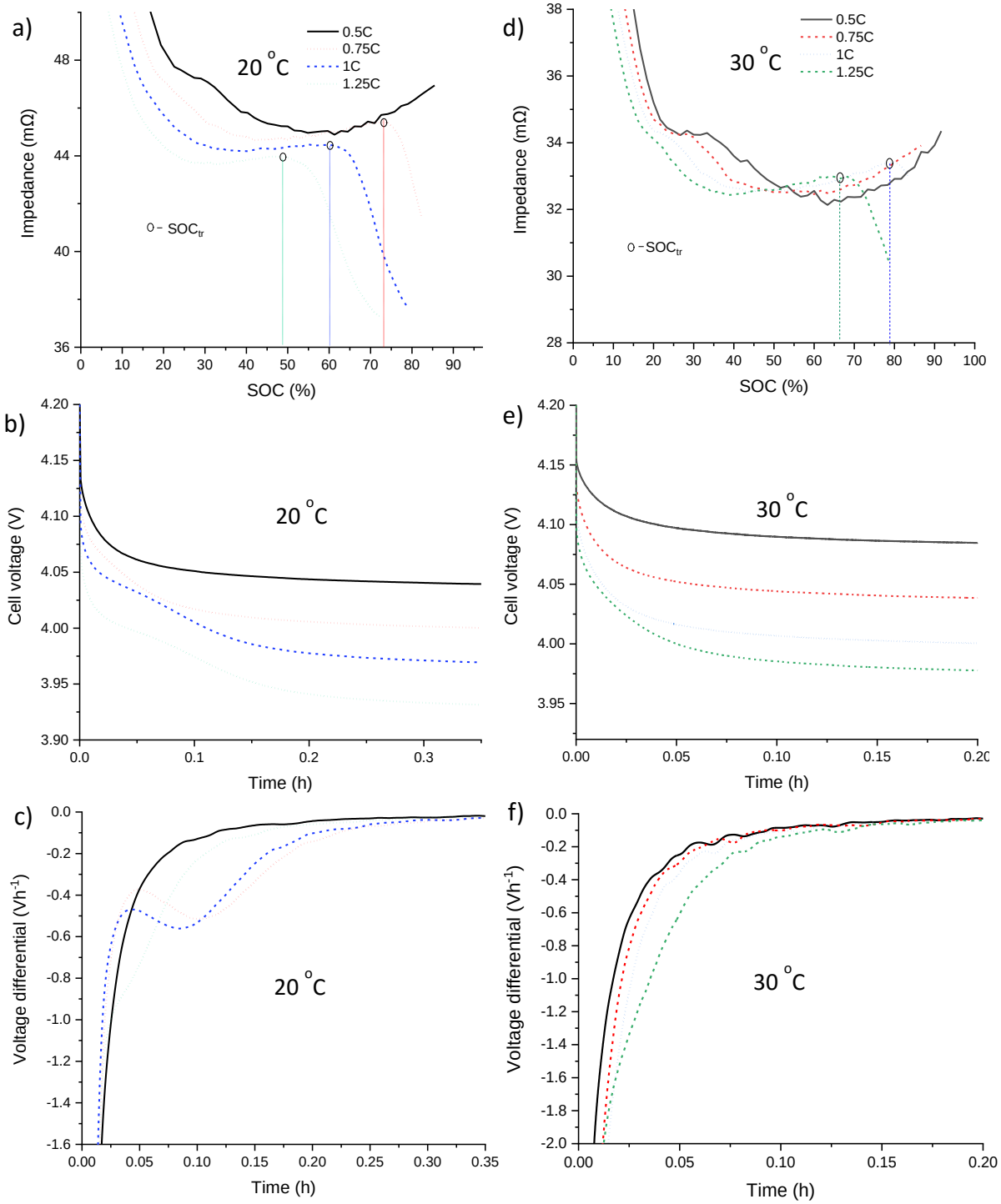

Figure 6: ZTR trends at different C-rates at a) 20 °C in test case B and d) 30 °C in test case C; Corresponding post-charge voltage relaxation profiles at b) 20 °C and e) 30 °C and c) and their differentials at c) 20 °C and f) 30 °C

4.3 Charge at high temperatures

Similar to test case A performed at 10 °C, the value of ZTR is tracked at high temperatures (20 and 30 °C) at different C-rates with the charge interruption procedure to verify the proposed method's effectiveness at higher ambient temperatures. Figure 6a, b and c show the ZTR trends, post-charge voltage relaxation

profiles and their differentials respectively at 20 °C for the test case B. As it can be seen from Figure 6a, for charge currents ≥0.75C, the ZTR profile shows a negative trend towards the end of CC charging. For these charge rates, differentials of the post-charge voltage relaxation profiles (Figure 6c) also show peak and valleys indicating a 2-stage recovery and thus confirming lithium-plating occurrence. Figure 6d, 6e and 6f show the ZTR trends, post-charge voltage relaxation profiles and their differentials respectively at ambient temperature of 30 °C for the test case C. From the ZTR profiles, it can be seen that lithium plating is occurring for the charge C-rates ≥ 1C. While the VRP method failed to indicate the occurrence of lithium plating for these charge rates.

The possible limitation of the VRP method within this context is discussed further within [23] and summarised below. There are two potential reasons for the VRP method's failure to indicate plating at high temperatures. First, as discussed within [41, 42], lithium plating levels reduce with increasing temperature and second, lithium-stripping rate increases with increasing temperature. The combined effect of decreasing lithium plating levels and increasing stripping rate reduces the stripping time. As discussed within [21], the VRP method often fails to detect plating when the lithium plating levels are below 2.5% of the battery capacity because it can become difficult to identify the 2-stage recovery in the time domain. However, the proposed ZTR based method validated at low 10 °C with the VRP method is able to detect the onset of plating even when the VRP failed at an ambient 30 °C temperature. This indicates that the proposed method is highly sensitive compared to the VRP method while having the ability to detect the onset of plating for a broader range of environmental conditions.

4.4 Sensitivity to Interruption time

For practical applications and for inclusion with the BMS, influence of the length of the rest period in tracking the ZTR are analysed to better define whether a reduced interruption time is still able to capture the ZTR profiles accurately. By extracting the voltages recovered in 0.25 s, 0.5 s, 1 s and 2 s of the 3 s recovery period, the ZTR is calculated at these intervals of recovery and shown graphically in Figure 7a (at 0.2C) and b (at 1C) in comparison with the 3 s data for the test case A. As it can be seen, the ZTR profiles appear similar albeit with some offset (circa 5 mΩ between the profiles observed at 3 and 0.25 s).

The reason for the ZTR profiles with offsets is analysed here. The selected reference f_{max} (0.1 Hz) is sufficiently lower than the actual f_{max} (> 3.4 Hz as can be seen from Figure 1c) of the new cells and therefore the impedance tracking approach captures not only the mid-frequency region but also a portion of the impedance from the low-frequency region. As the rest period is reduced from 3 s to 0.25 s, the contribution of the low-frequency region's impedance to the overall ZTR estimated value is equally reduced. Therefore, the ability to track the impedance from the mid-frequency region and thus detect the onset of lithium plating is still valid with the reduction of rest period by 12 times.

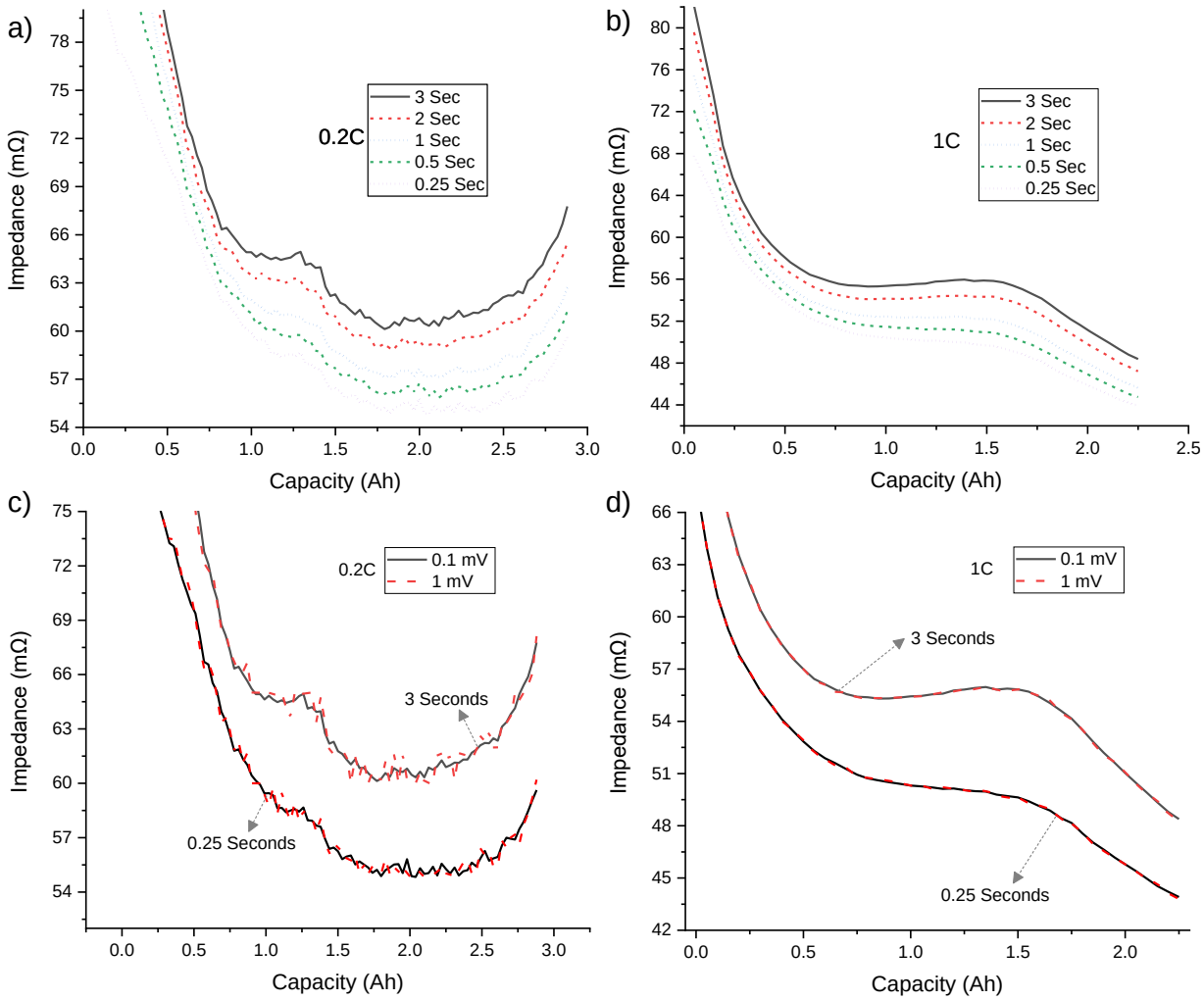

Figure 7: Impedance measurement sensitivity: a) Pulse period and b) Voltage resolution influence at 0.2C; c) Pulse and d) Voltage resolution influence at 1C

4.5 Sensitivity to voltage measurement resolution

Although the Maccor cell cycler enables voltage measurement with the resolution of 0.1 mV, it may be difficult to obtain such a high resolution in practical applications using typical BMS hardware. A 12 bit analogue to digital converter (ADC) that is found in a microcontroller can measure the voltage with the resolution of circa 1 mV (= 4200/2^12). To verify the proposed method's ability to track ZTR and detect lithium plating under practical scenarios where voltage resolution is limited by the ADCs, measured voltages are quantised to 1mV. Figure 7c and d show the ZTR profiles at 0.2C and 1C respectively at both resolution levels. ZTR calculated with 1 mV resolution at 0.2C in both 3 s and 0.25 s rest periods is similar to the 0.1 mV but with some additional noise added to the measurement. In the case of 1C, ZTR profiles are similar irrespective of the lower voltage resolution. Therefore, the reduced voltage resolution may not hinder the ZTR profile tracking methodology and thus detecting lithium plating in real-time applications.

4.6 Impact of minimal cooling

The EIS plots at different SOCs (Figure 1b) and ZTR profiles in test cases A, B and C are taken at constant ambient temperatures in which impedances from Ohmic, SEI layer and electrolyte are assumed to remain constant. However, in practical applications, temperature rise during a charging event is inevitable which can increase the Ohmic resistance and decrease the impedances due to electrolyte, CTL and SEI layer [28, 43]. Tracking the Z_{CTL} and thus detecting lithium plating may, therefore, become difficult if all the processes within the mid to high-frequency region are affected by temperature variations. To track the ZTR under the scenarios of minimal cooling, the cells from test case D are charged in a large room maintained at 20 ± 2 °C, but with no active thermal management. In each charge event, different C-rates are applied with pulse interruption procedure starting from 0.2C to 1.25C.

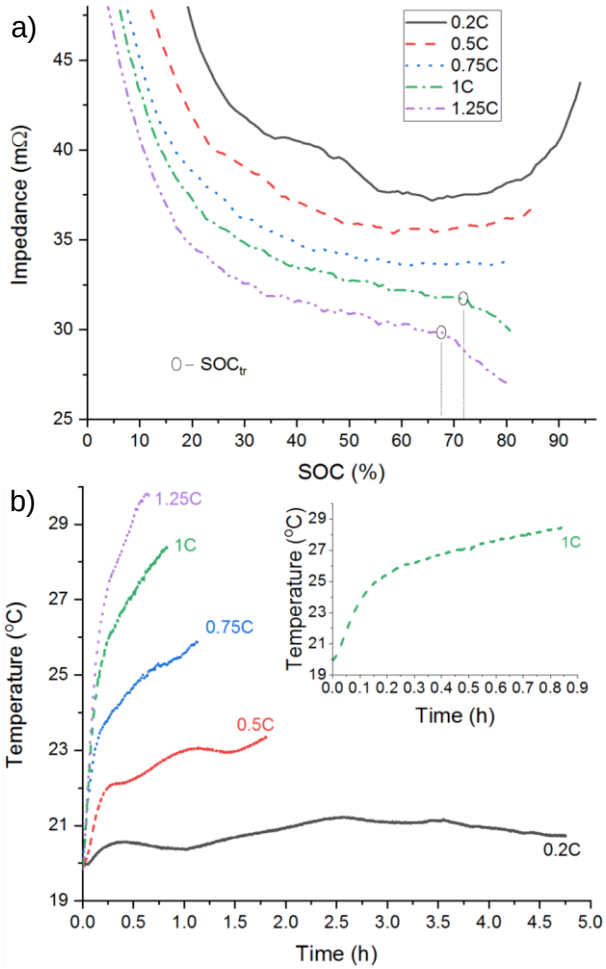

Figure 8: ZTR profiles without thermal cooling: a) ZTR profiles at different C-rates and b) temperature profiles measured on the cell surface

Figure 8a and 8b show the ZTR profiles and cell surface temperature variations on a cell at different charging C-rates. The ZTR profile at 0.2C where the temperature rise is within +1 °C is similar to the ZTR profiles observed with active cooling. With the increase of C-rate, lithium plating induced trend change in the ZTR profiles is clearly observed even with a temperature rise higher than 8 °C for charge rates ≥ 1C.

The ability to detect lithium plating using the ZTR profiles while temperature is also changing can be explained as follows. As seen from the inset plot in Figure 8b for 1C charge rate, the majority of the temperature rise (circa 5 ^{o}C rise of the total 8.2 ^{o}C) occurred during the first 10 minutes of the charging process and then the rate of temperature increase is reduced to circa 3.2 ^{o}C rise over the next 39 minutes. Since lithium plating typically occurs towards the end of CC charging where temperature changes are not assumed to be significant, temperature influence on the internal processes may be limited. Therefore, for the selected cell type and C-rates, lithium-plating detection using the ZTR profiles is possible even under environmental conditions where temperature is increased during the charge process

5 Future work and Conclusions

5.1. Future work

5.1.1 Optimization of the proposed method

As observed in this work, the shape of the ZTR profile indicates the presence or absence of lithium plating during a charging event. A reduction of interruption pulse length from 3 s to 0.25 is able to track the ZTR profile shape and identify the onset of lithium plating. Since the interruption procedure can influence the overall charging time, a further study is required to optimize the charge interruption interval to minimize undesirable increases in overall charge time whilst maintaining the ability to track the ZTR profile.

5.1.2 ZTR tracking in aged cells

Within this work, an initial study of a new concept to detect lithium plating is introduced and validated on new cells. The selected 3 s interruption period is able to track the ZTR for a new cell at different C-rates and ambient temperatures effectively. However, as discussed within [28], the f_{tr} and f_{max} reduce as the battery ages and thus the interruption time needs to be re-estimated and adjusted in line with battery ageing to track the ZTR. In addition, impedance levels of the internal processes within the battery are known to undergo changes as it degrades. Therefore, further work is required to study the robustness of the proposed method while cycling the cell as it loses capacity and its impedance characteristics change. Within such a study, to further validate the proposed method, the presence of lithium metal depositions can be verified by ex-situ means such as ICP-OES or NMR using the electrodes separated from the cycled cells.

5.1.3 Validation in different working conditions

As discussed within Section 4.7, the proposed method is able to detect lithium plating in cases where active cooling is not employed. A small variation in the cell surface temperature (for example, circa 3 ^{o}C rise in the last 50% of capacity addition at 1C rate) might have limited the contribution of temperature changes to the impedance variation. However, the cell surface temperature can significantly change and influence the impedance while charging in environments with time-variant temperature. To study the method's sensitivity to variations in ambient temperature, a further study is required.

5.1.4 Implementation within a BMS

Given the proposed method's dependency on the voltage and current measurements, it can be implemented in real-time applications. For this, control algorithms suitable for a BMS to detect and limit lithium-plating needs to be developed and evaluated. Within such a study, its ability to detect plating under different practical scenarios such as partial charge events and dynamic battery temperatures needs to be explored. Therefore, a further work is required to study the method's integration within a BMS.

5.1.5 Validation on different cell types

In this study, NCA/Graphite based 18650 cells are used to demonstrate the impedance-based lithium plating detection strategy. Since lithium plating is a phenomenon that occurs at the graphite electrode, the suggested method should work for all graphite-based lithium-ion cells. However, as discussed within [44] cell construction and chemistry can influence the internal processes and thus their impedance values. Since the method depends on tracking the impedance, a further study is required to verify the transferability of the method to different cell formats and chemistries.

5.2 Conclusions

In conclusion, lithium plating in commercial NCA/graphite cells when charged at different C-rates under diverse ambient conditions is studied. Since lithium plating diverts a portion of the charging current at the negative electrode, it introduces an effective parallel reaction across the NE intercalation. Experimental results highlight that tracking the impedance of the cell can be used to detect the onset of lithium plating. During charge at high C-rates, the ZTR impedance has been shown to deviate from the usual profile at a defined SOC threshold, indicating the onset of lithium plating, with a further reduction in impedance as the value of SOC progress towards 100%. Using the established VRP method as a benchmark, this technique has been proven to accurately detect the onset of lithium plating at different C-rates and ambient temperatures. This fact coupled with practical considerations such as the resolution of the voltage measurement and duration of the current interval implies that it is suitable to underpin the derivation of optimised charging strategies and for inclusion in a real-world BMS. Unlike the previously available lithium-plating detection methods that detect lithium plating after completion of the charge process, the proposed in situ impedance (ZTR) based lithium-plating detection method is able to detect the onset of lithium plating during charge itself. In addition, its ability to detect lithium plating at room temperatures will be useful to study the limitations of the fast charging more accurately at practical environmental operating conditions. These advantages are useful particularly for EVs since they will underpin the development of new innovative fast-charging profiles. Further work from this research is therefore focused on the derivation of novel charging strategies that optimise the trade-off between minimal degradation and charge time.

References

1. Bach, T.C., et al., *Nonlinear aging of cylindrical lithium-ion cells linked to heterogeneous compression.* Journal of Energy Storage, 2016. **5**: p. 212-223.
2. Günter, F.J., et al., *Introduction to Electrochemical Impedance Spectroscopy as a Measurement Method for the Wetting Degree of Lithium-Ion Cells.* Journal of The Electrochemical Society, 2018. **165**(14): p. A3249-A3256.
3. Uhlmann, C., et al., *In situ detection of lithium metal plating on graphite in experimental cells.* Journal of Power Sources, 2015. **279**: p. 428-438.
4. Legrand, N., et al., *Physical characterization of the charging process of a Li-ion battery and prediction of Li plating by electrochemical modelling.* Journal of Power Sources, 2014. **245**: p. 208-216.
5. Cicconi, P., et al., *A life cycle costing of compacted lithium titanium oxide batteries for industrial applications.* Journal of Power Sources, 2019. **436**.
6. Zhang, Q., et al., *Structural and electrochemical properties of Gd-doped Li4Ti5O12 as anode material with improved rate capability for lithium-ion batteries.* Journal of Power Sources, 2015. **280**: p. 355-362.
7. Nitta, N., et al., *Li-ion battery materials: present and future.* Materials Today, 2015. **18**(5): p. 252-264.
8. Gao, Y., et al., *Lithium-ion battery aging mechanisms and life model under different charging stresses.* Journal of Power Sources, 2017. **356**: p. 103-114.
9. Schmalstieg, J., et al., *A holistic aging model for Li(NiMnCo)O2 based 18650 lithium-ion batteries.* Journal of Power Sources, 2014. **257**: p. 325-334.
10. Waldmann, T., M. Kasper, and M. Wohlfahrt-Mehrens, *Optimization of Charging Strategy by Prevention of Lithium Deposition on Anodes in high-energy Lithium-ion Batteries – Electrochemical Experiments.* Electrochimica Acta, 2015. **178**: p. 525-532.
11. Gallagher, K.G., et al., *A Volume Averaged Approach to the Numerical Modeling of Phase-Transition Intercalation Electrodes Presented for LixC6.* Journal of the Electrochemical Society, 2012. **159**(12): p. A2029-A2037.
12. Smart, M.C. and B.V. Ratnakumar, *Effects of Electrolyte Composition on Lithium Plating in Lithium-Ion Cells.* Journal of The Electrochemical Society, 2011. **158**(4): p. A379.
13. Ren, D., et al., *Investigation of Lithium Plating-Stripping Process in Li-Ion Batteries at Low Temperature Using an Electrochemical Model.* Journal of The Electrochemical Society, 2018. **165 (10)** A2167-A2178
14. Yang, X.-G., et al., *Modeling of lithium plating induced aging of lithium-ion batteries: Transition from linear to nonlinear aging.* Journal of Power Sources, 2017. **360**: p. 28-40.
15. Lewerenz, M., A. Warnecke, and D.U. Sauer, *Post-mortem analysis on LiFePO 4 |Graphite cells describing the evolution & composition of covering layer on anode and their impact on cell performance.* Journal of Power Sources, 2017. **369**: p. 122-132.
16. Anseán, D., et al., *Operando lithium plating quantification and early detection of a commercial LiFePO 4 cell cycled under dynamic driving schedule.* Journal of Power Sources, 2017. **356**: p. 36-46.
17. Eckera, M., P.S. Sabeta, and D.U. Sauer, *Influence of operational condition on lithium plating for commercial lithium-ion batteries – Electrochemical experiments and post-mortem analysis.* Applied Energy. **206**: p. 934-946.
18. Klett, M., et al., *Non-uniform aging of cycled commercial LiFePO4//graphite cylindrical cells revealed by post-mortem analysis.* Journal of Power Sources, 2014. **257**: p. 126-137.
19. Frisco, S., et al., *Understanding Li-Ion Battery Anode Degradation and Pore Morphological Changes through Nano-Resolution X-ray Computed Tomography.* Journal of The Electrochemical Society, 2016. **163**(13): p. A2636-A2640.

20. Ge, H., et al., *Investigating Lithium Plating in Lithium-Ion Batteries at Low Temperatures Using Electrochemical Model with NMR Assisted Parameterization.* Journal of The Electrochemical Society, 2017. **164**(6): p. A1050-A1060.
21. von Lüders, C., et al., *Lithium plating in lithium-ion batteries investigated by voltage relaxation and in situ neutron diffraction.* Journal of Power Sources, 2017. **342**: p. 17-23.
22. Petzl, M. and M.A. Danzer, *Nondestructive detection, characterization, and quantification of lithium plating in commercial lithium-ion batteries.* Journal of Power Sources, 2014. **254**: p. 80-87.
23. Koleti, U.R., et al., *The development of optimal charging strategies for lithium-ion batteries to prevent the onset of lithium plating at low ambient temperatures.* Journal of Energy Storage, 2019. **24**.
24. Schindler, S., et al., *Voltage relaxation and impedance spectroscopy as in-operando methods for the detection of lithium plating on graphitic anodes in commercial lithium-ion cells.* Journal of Power Sources, 2016. **304**: p. 170-180.
25. Zinth, V., et al., *Lithium plating in lithium-ion batteries at sub-ambient temperatures investigated by in situ neutron diffraction.* Journal of Power Sources, 2014. **271**: p. 152-159.
26. Koleti, U.R., et al., *A new concept to improve the lithium plating detection sensitivity in lithium-ion batteries* International Journal of Smart Grid and Clean Energy 2019. **vol. 8, no. 5**: p. 505-516.
27. Singh, M., J. Kaiser, and H. Hahn, *Effect of Porosity on the Thick Electrodes for High Energy Density Lithium Ion Batteries for Stationary Applications.* Batteries, 2016. **2**(4): p. 35.
28. Waag, W., S. Käbitz, and D.U. Sauer, *Experimental investigation of the lithium-ion battery impedance characteristic at various conditions and aging states and its influence on the application.* Applied Energy, 2013. **102**: p. 885-897.
29. Itagaki, M., et al., *In-situ EIS to determine impedance spectra of lithium-ion rechargeable batteries during charge and discharge cycle.* Journal of Electroanalytical Chemistry, 2015. **737**: p. 78-84.
30. Pinson, M.B. and M.Z. Bazant, *Theory of SEI Formation in Rechargeable Batteries: Capacity Fade, Accelerated Aging and Lifetime Prediction.* Journal of the Electrochemical Society, 2012. **160**(2): p. A243-A250.
31. Kassem, M., et al., *Calendar aging of a graphite/LiFePO4 cell.* Journal of Power Sources, 2012. **208**: p. 296-305.
32. von Srbik, M.-T., et al., *A physically meaningful equivalent circuit network model of a lithium-ion battery accounting for local electrochemical and thermal behaviour, variable double layer capacitance and degradation.* Journal of Power Sources, 2016. **325**: p. 171-184.
33. Lundgren, H., et al., *Thermal Management of Large-Format Prismatic Lithium-Ion Battery in PHEV Application.* Journal of The Electrochemical Society, 2015. **163**(2): p. A309-A317.
34. Hariharan, K.S. and V. Senthil Kumar, *A nonlinear equivalent circuit model for lithium ion cells.* Journal of Power Sources, 2013. **222**: p. 210-217.
35. Cho, S., et al., *State-of-charge estimation for lithium-ion batteries under various operating conditions using an equivalent circuit model.* Computers & Chemical Engineering, 2012. **41**: p. 1-9.
36. Gordon, I.J., et al., *Original implementation of Electrochemical Impedance Spectroscopy (EIS) in symmetric cells: Evaluation of post-mortem protocols applied to characterize electrode materials for Li-ion batteries.* Journal of Power Sources, 2016. **307**: p. 788-795.
37. Stroe, D.-I., et al., *Generalized Characterization Methodology for Performance Modelling of Lithium-Ion Batteries.* Batteries, 2016. **2**(4): p. 37.
38. Dubarry, M., et al., *Evaluation of commercial lithium-ion cells based on composite positive electrode for plug-in hybrid electric vehicle applications. Part I: Initial characterizations.* Journal of Power Sources, 2011. **196**(23): p. 10328-10335.
39. Chu, Z., et al., *Non-destructive fast charging algorithm of lithium-ion batteries based on the control-oriented electrochemical model.* Applied Energy, 2017. **204**: p. 1240-1250.
40. Bitzer, B. and A. Gruhle, *A new method for detecting lithium plating by measuring the cell thickness.* Journal of Power Sources, 2014. **262**: p. 297-302.
41. Burns, J.C., D.A. Stevens, and J.R. Dahn, *In-Situ Detection of Lithium Plating Using High Precision Coulometry.* Journal of the Electrochemical Society, 2015. **162**(6): p. A959-A964.

42. Waldmann, T., et al., *Interplay of Operational Parameters on Lithium Deposition in Lithium-Ion Cells: Systematic Measurements with Reconstructed 3-Electrode Pouch Full Cells.* Journal of The Electrochemical Society, 2016. **163**(7): p. A1232-A1238.
43. Mathew, M., et al., *Comparative Analysis of Lithium-Ion Battery Resistance Estimation Techniques for Battery Management Systems.* Energies, 2018. **11**(6).
44. Vogel, J.E., et al., *Electrode microstructure controls localized electronic impedance in Li-ion batteries.* Electrochimica Acta, 2019. **297**: p. 820-825.